GT2024-125711

ADJOINT BASED SHAPE OPTIMIZATION FOR THERMOACOUSTIC STABILITY OF COMBUSTORS USING FREE FORM DEFORMATION

Ekrem Ekici[1], Matthew P. Juniper[1,*]

[1]Department of Engineering, University of Cambridge, Cambridge, United Kingdom, CB21PZ

ABSTRACT

We use the thermoacoustic Helmholtz equation to model thermoacoustic oscillations as an eigenvalue problem. We solve this with a Finite Element method. We parameterize the geometry of an annular combustor geometry using Free Form Deformation (FFD). We then use the FFD geometry, define the system parameters and impose the acoustic boundary conditions to calculate the eigenvalue and eigenvector of the problem using a Helmholtz solver. We then use adjoint methods to calculate the shape derivatives of the unstable eigenvalue with respect to the FFD control points. According to these gradients, we propose modifications to the control points that reduce the growth rate. We first demonstrate the application of this approach on the Rijke tube. Then we extend the method to a simulation of a laboratory combustor and lower the growth rate of the unstable circumferential mode. These findings show how this method could be used to reduce combustion instability in industrial annular combustors through geometric modifications.

Keywords: thermoacoustic instability, design optimization, FEM, Gas turbine combustor

NOMENCLATURE
Roman letters
c Speed of sound [m s^{-1}]
u_b Mean velocity [m s^{-1}]
q_0 Mean heat release rate [W]
$\hat{p}_1$ Acoustic pressure [N m^{-2}]
$\bar{p}_{gas}$ Mean pressure [N m^{-2}]
$\hat{\mathbf{u}}$ Acoustic velocity [m s^{-1}]
M Mach number [-]
Z Specific impedance [-]
R Reflection coefficient [-]
T_0 Temperature [K]
r_{gas} Universal gas constant [J/kg K^{-1}]
Greek letters
ω Angular eigenfrequency [rad s^{-1}]

γ Heat capacity ratio [-]
τ time delay [s^{-1}]
κ curvature [-]
Superscripts and subscripts
$\hat{()}_1$ perturbed quantities
$()^\dagger$ adjoint variables
$()^*$ complex conjugate
$()_b$ bulk quantities
$()_u$ upstream
$()_d$ downstream
$()_{in}$ inlet
$()_{out}$ outlet
$()_{tot}$ total
$()_i$ the index of the control point in the radial direction
$()_j$ the index of the control point in the circumferential direction
$()_k$ the index of the control point in the axial direction

1. INTRODUCTION

Thermoacoustic instability is a major problem that threatens the sustainable operability of gas turbine engines. Growing acoustic oscillations in the combustor chamber can lead to detrimental vibrations that increase the fatigue of engine components. These oscillations are extremely sensitive to minor changes in some system parameters, such as operating point, fuel composition and system geometry [1]. The sensitivities to the boundary conditions, mean temperature gradient, mean Mach number, and interaction index of the thermoacoustic system are examined in [2] through a parametric study of a one-dimensional Galerkin expansion model. Regarding the geometrical sensitivities, a database and design strategies for suppressing acoustic oscillations by changing the geometrical parameters are examined in [3] and [4] by focusing on the burner shape. In addition to the parametric and experimental studies, relatively cheap and accurate tools are desirable to examine the influence of the design parameters.

To determine the sensitivity to system parameters, adjoint methods can be used [5]. With adjoint methods, the behaviour

*Corresponding author: mpj1001@cam.ac.uk

of the eigenvalue with respect to the system parameters can be calculated cheaply. In addition to the operating parameters, geometrical parameters of the combustor can be considered. The motivation is that small modifications to the geometry could lead to passive control of the system [6]. A low-order network model is used in [7] to stabilize the unstable modes of a longitudinal combustor by changing its shape, informed by adjoint methods. The same approach is applied to the annular combustor geometry in [8] by making small changes in radii, cross-sectional areas and lengths over the modules within the network model of the thermoacoustic system. However, low-order thermoacoustic network models are limited to relatively simple combustor geometries. For this reason, more complex geometries are better analysed with Helmholtz solvers, at the cost of increased computational effort. In Helmholtz solvers, the mean flow is assumed to be zero, and the fluctuating heat release rate is modelled as a distributed acoustic source.

Adjoint methods give the sensitivity of the thermoacoustic eigenvalue to generic geometry changes. It is helpful to parameterize the geometry of a combustor and then to find the sensitivity to changes in those parameters. This creates a smaller and better posed optimization problem. Helmholtz solvers are well-suited to handle complex combustor geometries, such as those in aircraft gas turbines. The parametrization of thermoacoustic system geometries were first examined for a two dimensional Rijke tube with B-Splines in [6]. Next, this method was extended to a relatively complex academic combustor, MICCA, with a Non-Uniform Rational B-Splines (NURBS) parametrization [9]. When dealing with realistic geometries, however, the necessity for a parametrization tool capable of managing both local and global parametrization across various components becomes apparent. Using free form deformation (FFD) allows us to handle any geometry and allows us to control the degree of local or global parametrization complexity. This method is first introduced in [10] to increase the modelling capabilities and the representation accuracy of the surfaces of solid bodies in a free-form manner. With a free-form lattice formed by a few control points, the FFD technique offers the sensitivity to local and global deformations of the embedded geometry through control point displacements. In addition to computer graphics, the effectiveness of FFD to handle complex geometries has made it a strong candidate to improve structural designs in industry. One of the first examples of FFD is found in aerodynamic shape optimization problems in [11] and has recently been applied to airfoil geometries with adaptive parametrization techniques [12]. For turbomachinery applications, FFD has been combined with adjoints in order to optimize a jet-engine fan blade [13]. In gas turbine engines, the applications of FFD can be found for compressor [14] and turbine [15] designs but not for the combustor. Here, we propose a lattice-based FFD technique to examine the sensitivity of thermoacoustic instability to changes in the combustor geometry.

In this study, we apply the FFD technique to combustor geometries to reduce the thermoacoustic growth rate by making geometrical changes. We use an adjoint Helmholtz solver to calculate the sensitivity of the thermoacoustic eigenmodes to changes in the FFD control points surrounding the parametrized geometry. We use the finite element method to handle the three-dimensional

complex geometries. The nonlinear eigenvalue problem is solved using fixed point iteration. The direct and adjoint eigenfunctions are used to calculate the shape derivatives of the FFD control points.

2. METHODOLOGY

2.1 Thermoacoustic Helmholtz Equation

The derivation of the direct and adjoint thermoacoustic Helmholtz equations follows the methodology in [16]. The direct Helmholtz equation and momentum equation are

$$\nabla \cdot \left(c^2 \nabla \hat{p}_1 \right) + \omega^2 \hat{p}_1 = i\omega(\gamma - 1)\hat{q}_1(\omega) \tag{1a}$$

$$-i\rho_0 \omega \hat{\mathbf{u}}_1 + \nabla \hat{p}_1 = 0, \tag{1b}$$

where c is the spatially-varying speed of sound, $\hat{p}_1$ is the acoustic pressure, $\hat{\mathbf{u}}$ is the acoustic velocity, ω is the complex valued angular frequency, γ is the heat capacity ratio, $\hat{q}_1$ is any fluctuating heat release rate and p_0 is the mean pressure. Eq. (1) can be written as $\mathcal{L}(\omega)\hat{p}_1 = 0$, where $\mathcal{L}$ is a differential operator that is linear in $\hat{p}_1$ but potentially nonlinear in ω. The local $n - \tau$ formulation is used to model the heat release rate caused by the unsteady flame response:

$$\frac{q_1(\mathbf{x}, t)}{\bar{q}_0} = \frac{nh(\mathbf{x}) \int_\Omega w(\mathbf{x})\hat{\mathbf{u}}\left(\mathbf{x}, t - \tau(\mathbf{x})\right) \cdot \mathbf{n}_r \, d\mathbf{x}}{\bar{u}_b} \tag{2}$$

where $\bar{q}_0$ is the mean heat release rate, n is the interaction index, $\bar{u}_b$ is the mean velocity, τ is the time delay and $\mathbf{n}_r$ is the unit normal vector in the reference direction. $h(\mathbf{x})$ and $w(\mathbf{x})$ are the heat release rate distribution and measurement function fields, which are modified Gaussian functions integrating to 1 over the domain.

With the definition $\langle \hat{p}_1^\dagger | \mathcal{L}\hat{p}_1 \rangle + b.t. = 0$, the adjoint Helmholtz equation and momentum equations are [16]

$$\nabla \cdot \left(c^2 \nabla \hat{p}_1^\dagger \right) + \omega^{*2} \hat{p}_1^\dagger = i\omega^*(\gamma - 1)\hat{q}_1(\omega^*) \tag{3a}$$

$$-i\rho_0 \omega^* \hat{\mathbf{u}}_1 + \nabla \hat{p}_1^\dagger = 0. \tag{3b}$$

where $\hat{p}_1^\dagger$ is the adjoint eigenfunction and w^* is the complex conjugate of the angular eigenfrequency.

2.2 Boundary Conditions

Three types of acoustic boundary conditions are used: Dirichlet, Neumann and Robin conditions. For annular combustors, most of the walls are Neumann ($\nabla \hat{p}_1 \cdot \mathbf{n} = 0$) and Robin boundaries. Reflection coefficients can be imposed on Robin boundaries through the specific impedance, $Z = (1 + R)/(1 - R)$:

$$\nabla \hat{p}_1 \cdot \mathbf{n} - \frac{iw}{cZ} \hat{p}_1 = 0 \tag{4}$$

for the direct solution and

$$\nabla \hat{p}_1^\dagger \cdot \mathbf{n} - \frac{iw^*}{cZ} \hat{p}_1^\dagger = 0 \tag{5}$$

for the adjoint solution.

For annular combustors, most of the walls are Neumann ($\nabla \hat{p}_1 \cdot \mathbf{n} = 0$) boundaries or choked boundary conditions. The reflection coefficient of the inlet choked boundary condition is

$$R_{in} = \frac{1 - \gamma_i \bar{M}_{in}/(1 + (\gamma_i - 1)\bar{M}_{in}^2)}{1 + \gamma_{in} \bar{M}_{in}/(1 + (\gamma_{in} - 1)\bar{M}_{in}^2)}, \tag{6}$$

where γ_{in} is the heat capacity ratio on the inlet choked boundary and $\bar{M}_{in}$ is the Mach number near the downstream of the inlet choked boundary. Similarly, we write the choked outlet condition as

$$R_{out} = \frac{1 - (\gamma_{out} - 1)\bar{M}_{out}/2}{1 + (\gamma_{out} - 1)\bar{M}_{out}/2}, \tag{7}$$

where γ_{out} is the heat capacity ratio on the outlet choked boundary and $\bar{M}_{out}$ is the Mach number near the upstream of the outlet choked boundary. These reflection coefficients can be imposed on Robin boundaries through the specific impedance, $Z = (1 + R)/(1 - R)$ [17].

2.3 Finite Element Formulation

Within the finite element framework, we integrate the terms in (1a) over the domain and multiply by a test functions ϕ_j such that $v = \sum_j \phi_j$ to obtain

$$\sum_j \left(\int_\Omega \nabla \cdot \left(c^2 \nabla \hat{p}_1 \right) \cdot \phi_j \, \mathbf{dx} + \int_\Omega \omega^2 \hat{p}_1 \cdot \phi_j \, \mathbf{dx} \right) = \\ \sum_j \left(\int_\Omega i\omega(\gamma - 1)\hat{q}_1 \cdot \phi_j \, \mathbf{dx} \right) \tag{8}$$

We use trial functions ϕ_i such that $\hat{p}_1 = \sum_i \phi_i \cdot p_{1,i}$. Integrating the terms in Eq. (8) by parts gives

$$\sum_i \left(\sum_j \left(- \int_\Omega c^2 \nabla \phi_i \cdot \nabla \phi_j \, \mathbf{dx} + \int_{\partial\Omega} c^2 (\nabla \phi_i \cdot \mathbf{n}) \, \phi_j \, dS \right. \right. \\ \left. \left. + \int_\Omega \omega^2 \phi_i \cdot \phi_j \, \mathbf{dx} \right) \right) p_{1,i} = \sum_i \left(\sum_j \left(\int_\Omega i\omega(\gamma - 1)\hat{q}_1 \cdot \phi_j \, \mathbf{dx} \right) \right) \tag{9}$$

where $\mathbf{n}$ is the normal vector of the relevant boundary. We can transform the second integral in Eq. (9) into the Robin integral using Eq. (4) by writing

$$\int_{\partial\Omega} c^2 (\nabla \phi_i \cdot \mathbf{n}) \, \phi_j \, dS = \int_{\partial\Omega} c^2 (\frac{iw}{cZ}\phi_i) \, \phi_j \, dS \tag{10}$$

The matrix form of Eq. (9) becomes

$$\left[\mathbf{A} + \omega \mathbf{B} + \omega^2 \mathbf{C} \right] \mathbf{p} = \mathbf{D}(\omega)\mathbf{p} \tag{11}$$

where

$$\mathbf{A} = -\int_\Omega c^2 \nabla \phi_i \cdot \nabla \phi_j \, \mathbf{dx}, \tag{12a}$$

$$\mathbf{B} = \int_{\partial\Omega} \frac{ic}{Z} \phi_i \cdot \phi_j \, dS, \tag{12b}$$

$$\mathbf{C} = \int_\Omega \phi_i \cdot \phi_j \, \mathbf{dx}, \tag{12c}$$

$$\mathbf{D} = \int_\Omega (\gamma - 1) \frac{q_0}{u_b} \; h \, n \, e^{i\omega\tau} \phi_j \mathbf{dx} \int_\Omega \frac{w(\mathbf{x})}{\rho_0} \, \nabla \phi_i \cdot \mathbf{n}_r \mathbf{dx} \tag{12d}$$

and $\mathbf{p}$ is the direct eigenvector. In Eq. (12d), there is an outer product between the left integral and the right integral. To derive the adjoint in matrix form, we take the conjugate transpose of Eq. (12) and calculate the right eigenvector to give the adjoint eigenvector.

2.4 Helmholtz solver

Three dimensional computational grids are generated by Gmsh [18] using Delaunay triangulation. The finite element model is built with the open-source platform DOLFINx [19] using P2 continuous Galerkin elements. The weak forms in Eq. (12) are defined using the UFL package [20]. All the matrices in Eq. (12) are assembled within the subroutines of DOLFINx apart from the active flame matrix. This matrix is implemented using the PETSc package [21] explicitly. The PEP solver in the SLEPc package [22] is used to determine the nonlinear quadratic eigenvalue problem (Eq. (11)). The shift-and-invert spectral transformation is exploited to enhance the convergence of the eigenvalue to the initial guess. Fixed point iteration with relaxation is implemented in order to converge to the eigenvalue [23]. The solver parallelizes with the OpenMPI library [24].

3. SHAPE PARAMETRIZATION

The geometry of the thermoacoustic system was parametrized with NURBS surfaces in our previous paper [9]. However, manipulation of more complex geometries requires extra care and we would like the parametrization approach to be applicable to any combustor shape. For this reason, we investigate the free form deformation technique to control the combustor geometries. In this section, we present the established free form deformation technique [10].

3.1 Free Form Deformation

Free form deformation creates a parametrization link between the mesh nodes and some control points. These control points form the control lattice (Fig. 1) and that lattice can take any geometric shape. In general, cylindrical or cube-shaped lattices are preferred in order to manipulate the control points more conveniently. Any point within the control lattice can be represented by parametric coordinates (s, t, u) as in Eq. (13), where $\mathbf{X}_0$ denotes the center of the FFD lattice and $\mathbf{S}$, $\mathbf{T}$ and $\mathbf{U}$ are the parametric unit vectors in the radial, circumferential and axial directions, respectively.

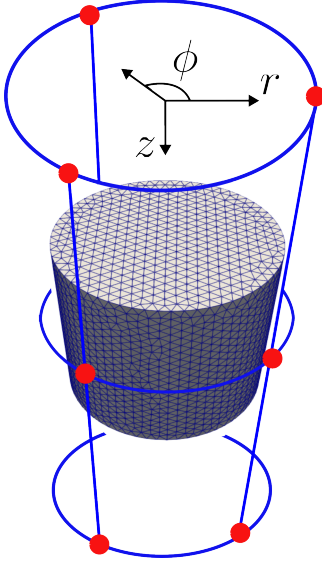$$\mathbf{X} = \mathbf{X}_0 + s\mathbf{S} + t\mathbf{T} + u\mathbf{U} \tag{13}$$

FIGURE 1: Free form deformation (FFD) configuration for a cylinder mesh using a cylindrical control lattice with control points (red dots). r, ϕ **and** z **denotes the radial, circumferential and axial directions. Blue lines visualize the connections between the control points.**

Considering the lattice in Fig. 1, the mesh nodes are initially transformed into cylindrical coordinates and then their parametric coordinates are calculated with Eq. (13). The range of the parametric coordinates is between 0 and 1 for radial (r) and axial (z) directions and between 0 and 2π for the azimuthal direction (ϕ).

The position of the FFD control points can be arbitrarily defined according to the application. In this paper, we specify the positions of the control points in a equispaced pattern within a cylindrical lattice using Eq. (14).

$$\mathbf{P}_{ijk} = \mathbf{X}_0 + \frac{i}{l}\mathbf{S} + \frac{j}{m}\mathbf{T} + \frac{k}{n}\mathbf{U} \qquad (14)$$

The locations and number of FFD control points are crucial because they form the control lattice and determine the allowable deformation magnitudes and directions. Therefore, the control points should be numbered and positioned to prevent or minimize potential overlapping deformations resulting from control point displacements. For simple or symmetric geometries, equispaced control points can manage the deformations. However, for complex shapes, an irregular pattern for the placements might work better depending on the aim of the application. For instance, control points forming a cylindrical lattice could handle cylinder-like geometries better, whereas cornered geometries might benefit from box-like lattices with control points positioned at the corners.

After specifying the lattice positions of the FFD control points and calculating the parametric coordinates of the mesh nodes, we are then ready to deform the geometry. We first displace the positions of the FFD control points and deform the mesh nodes individually with trivariate Bernstein basis polynomials, as shown in Eq. (15).

$$\mathbf{X}_{FFD} = \Bigg(\sum_{i=0}^{l}\binom{l}{i}(1-s)^{l-i}s^i$$
$$\Big(\sum_{j=0}^{m}\binom{m}{j}(1-t)^{m-j}t^j \qquad (15)$$
$$\Big(\sum_{k=0}^{n}\binom{n}{k}(1-u)^{n-k}u^k\mathbf{P}_{ijk}\Big)\Big)\Bigg)$$

In shape derivative calculations, the displacement field $\mathbf{V}_{ijk}$ is required for the control point $\mathbf{P}_{ijk}$. Taking the derivative of the mesh nodes with respect to the control point gives the displacement field, as shown in Eq. (16).

$$\frac{\partial}{\partial \mathbf{P}_{ijk}}\big(\mathbf{X}_{ffd}\big) = \mathbf{V}_{ijk} = \Bigg(\sum_{i=0}^{l}\binom{l}{i}(1-s)^{l-i}s^i$$
$$\Big(\sum_{j=0}^{m}\binom{m}{j}(1-t)^{m-j}t^j \qquad (16)$$
$$\Big(\sum_{k=0}^{n}\binom{n}{k}(1-u)^{n-k}u^k\Big)\Big)\Bigg)$$

The displacement field $\mathbf{V}_{ijk}$ can then be used in Eq. (17) for calculating the shape derivative of the control point $\mathbf{P}_{ijk}$.

3.2 Shape Derivatives

The shape sensitivities for the thermoacoustic Helmholtz equation are derived in [16]. With direct and adjoint eigenvectors, we can compute the shape derivative of the FFD control points in Hadamard-form. The most general expression for the shape derivative is that using Robin boundary conditions:

$$\omega'_{ijk} = \int_{\Gamma} \mathbf{V}_{ijk} \cdot \mathbf{n}_{ijk}\Bigg(-\hat{p}_1^{\dagger*}\Big(\kappa c^2\frac{\partial c}{\partial n}\Big)\frac{\partial \hat{p}_1}{\partial n} + \nabla\cdot\Big(\hat{p}_1^{\dagger*}c^2\nabla\hat{p}_1\Big)$$
$$-2\frac{\partial \hat{p}_1^{\dagger*}}{\partial n}c^2\frac{\partial \hat{p}_1}{\partial n}\Bigg)dS \qquad (17)$$

where ω'_{ijk} is the complex-numbered shape derivative for the control point $\mathbf{P}_{ijk}$ and $\mathbf{n}_{ijk}$ is its outward normal vector. When applying Neumann boundaries, we impose $\partial \hat{p}_1/\partial n = 0$ and $\partial \hat{p}_1^{\dagger}/\partial n = 0$. For degenerate cases, in which two identical eigenvalues correspond to two different thermoacoustic eigenfunctions, we use the formula [9];

$$\Bigg(\int_{\Gamma_1}\mathbf{V}_{ijk}\cdot\mathbf{n}_{ijk}\,G\big(\hat{p}_{1,a}^{\dagger},\hat{p}_{1,b}\big)dS - \omega'_{ijk}\delta_{ab}\Bigg) = 0 \qquad (18)$$

where G states the expression of Eq. (17) depending on the boundary condition and subscripts $_{1,a}$ and $_{1,b}$ denote the biorthonormal cases of Eq. (18). Hence, the shape derivative of the FFD control point for the degenerate case is the eigenvalue of Eq. (18).

As we compute the gradient information in the direction of the outward normal vector of the pertinent control point, the

significance of the complex component of the shape gradient becomes pivotal. In cases in which the computed mode is unstable and the complex part of the shape derivative at the control point bears a negative sign, displacing the control point in the outward normal vector direction will make the system more stable. On the other hand, if the imaginary part of the shape derivative for the control point has a positive value, adjusting the control point towards the inward normal vector direction makes the system more stable.

The steps of the shape optimization procedure using free form deformation can be summarized as follows:

- The three dimensional mesh is generated.

- The FFD lattice and control points are defined after calculation of the parametric coordinates of the mesh nodes.

- Direct and adjoint eigenmodes are calculated with degree 2 finite elements.

- The shape derivatives of the FFD control points are calculated and normalized.

- The shape is deformed following the direction provided by the shape derivatives, with a certain step size.

4. RESULTS

4.1 Rijke Tube

4.1.1 Geometry and FFD Setup. We start with the canonical example of thermoacoustic instability, the Rijke tube. We consider a cylinder with length 1.0m and diameter 0.047m, as in [1]. The three-dimensional mesh is generated with $25,246$ elements using Delaunay-triangulation by Gmsh [18]. The global FFD setup for the Rijke tube can be seen in Fig. 2. We place more control points in the axial direction in order to increase our control over the tube geometry.
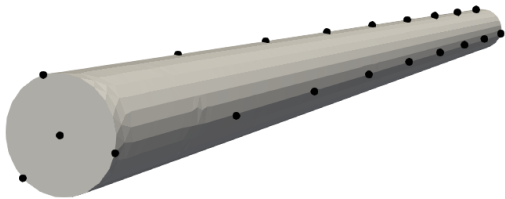

FIGURE 2: Control points (black dots) and external surface (grey) of the Rijke tube in this paper. There are 2, 3 and 9 control points in the radial, circumferential and axial directions respectively.

4.1.2 Parameters. The parameters for the Rijke tube problem are tabulated in Table 1. The heat release rate distribution and measurement function distribution are implemented by means of a three dimensional Gaussian function in Eq. (19), where α denotes the standard deviation, which controls the width of the function around point $P(x_0, y_0, z_0)$. The center of the heat source and measurement function distributions are located at $\mathbf{x}_f = (0, 0, 0.2)$ and $\mathbf{x}_r = (0, 0, 0.25)$ respectively. The relationship between the

heat release rate and acoustic velocity at the measurement point is defined through an $n - \tau$ model [23].

$$G(\mathbf{x}) = \frac{\exp\left(-\left((x - x_0)^2 + (y - y_0)^2 + (z - z_0)^2\right)/(2\alpha^2)\right)}{\alpha^3(2\pi)^{3/2}}$$
(19)

The speed of sound field changes in the axial direction at the loca-

TABLE 1: Dimensional parameters of the Rijke tube problem taken from [1]

Parameter	value	unit
r_{gas}	287.1	$\mathrm{Jkg^{-1}K^{-1}}$
$\bar{p}_{gas}$	100	kPa
$\bar{\rho}_u$	1.22	kg m^{-3}
$\bar{\rho}_d$	0.85	kg m^{-3}
$\bar{q}_0$	200	W
$\bar{u}_b$	0.1	m s^{-1}
n	0.014	-
τ	0.0015	s
γ	1.4	-
α_r	0.025	-
α_f	0.025	-
R_{in}	- 0.975 - 0.05j	-
R_{out}	- 0.975 - 0.05j	-

tion $\mathbf{x}_f$. Using upstream and downstream densities with the ideal gas law, the distribution of the speed of sound can be determined through the equation $c = \sqrt{\gamma r_{gas} T_0}$. Robin boundary conditions are imposed through reflection coefficients for the inlet and outlet boundaries and the lateral boundary is assumed to be a perfectly reflecting (Neumann) surface.

4.1.3 Eigenmode. Based on the parameters in Table 1, the first axial unstable eigenmode of the Rijke tube is computed. The corresponding eigenfunction is shown in Fig.3 with the eigenfrequency of $184.101 + 0.137i$ s^{-1}, which agrees with [1].
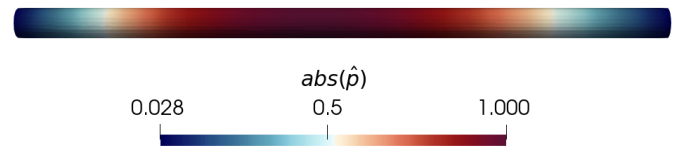

FIGURE 3: Normalized amplitude of the first axial mode of the Rijke tube. The corresponding eigenfrequency is $\omega/2\pi = f = 184.101 + 0.137i$ s^{-1}

4.1.4 Shape Modification. After obtaining the direct and adjoint eigenmodes of the Rijke tube, we calculate the shape derivatives of the control points on the lateral (Neumann) surface using Eq. (17). We prohibit axial shape changes and only allow radial displacements of the control points. As an example, the radial displacement field for the control control point $\mathbf{P}[2, 2, 5]$ is shown in Fig. 4. We iterate over the control points on the lateral boundary and move them individually in the direction indicated by the shape gradients. The resulting deformed geometry of the
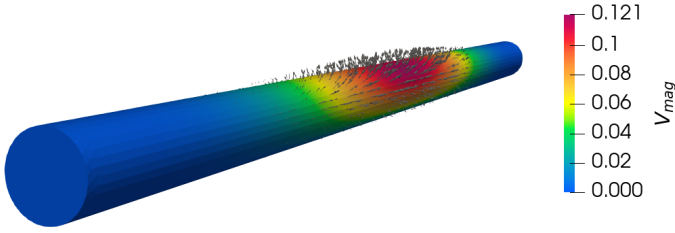
FIGURE 4: Deformation field of the Rijke tube for the control point $P[i, j, k]$ where $i = 2$, $j = 2$, $k = 5$. The colormap shows the magnitude of the displacement field. Some of the magnitude-scaled outward normal vectors of the mesh nodes are visualized on the lateral surface.

Rijke tube is shown in Fig. 5. The growth rate of the deformed design become negative after a few deformations. The trend of the growth rate due to deformation is similar to that in [6]. The example in this paper, however, allows radii changes for the inlet and outlet circular surfaces.

FIGURE 5: Optimized geometry of the Rijke tube. The eigenfrequency after free form deformation is $\omega/2\pi = f = 198.437 - 0.431$ s^{-1}. The black (top) and green (bottom) dots are the initial and final positions of the FFD control points for the initial (top) and final (bottom) geometries after few deformations.

4.2 Annular Combustor
4.2.1 Geometry and FFD Setup. For this subsection, we extend the shape optimization procedure to a more complex combustor geometry. We consider the lean premixed prevaporized (LPP) aeroengine combustor in [8, 25]. The sector view of this combustor is shown in Fig. 6 with dimensions of the annular geometry. It has a plenum, 20 premixed ducts and a combustion chamber, as well as cylindrical flame volumes.

The cylindrical FFD setup for the LPP is visualized in Fig. 7. For this annular geometry we generate two local cylindrical lattices, to increase the control over the plenum and combustion chamber geometries separately. The numbers of localized FFD control points are tabulated in Table 2. We place more control points over the combustion chamber because it is longer than the plenum. Similar to [9], we generate the annulus mesh for the plenum and combustion chamber geometries first, and then define a premix duct. Next, we copy and rotate that premix duct geometry 20 times and fuse the geometries. Lastly, we generate a three-dimensional unstructured mesh with $137,060$ elements and optimize it using the Netgen optimizer [18].

4.2.2 Parameters. The parameters for the LPP combustor are taken from [8, 25] and listed in Table 3. The mean temper-
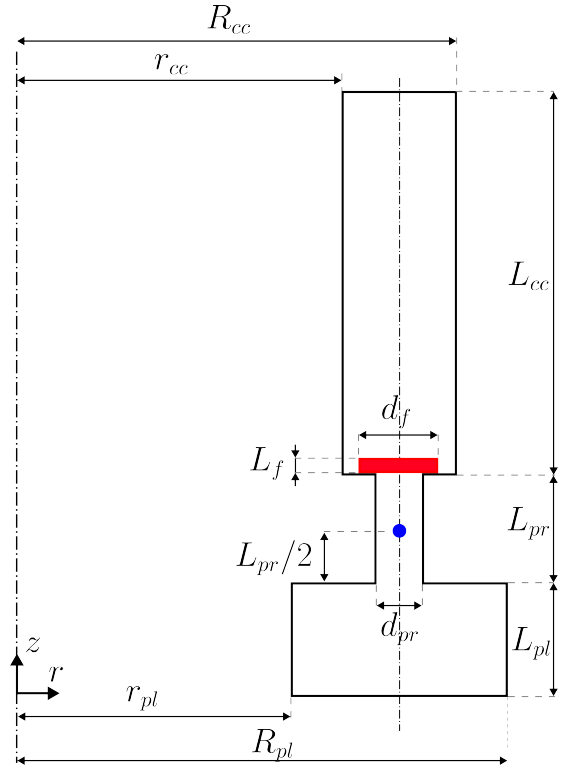

FIGURE 6: A section of one sector of the LPP combustor with $r_{pl} = 0.22$ m, $R_{pl} = 0.38$ m, $L_{pl} = 0.1$ m, $d_{pr} = 0.03568$ m, $L_{pr} = 0.1$ m, $d_f = 0.072$ m, $L_f = 0.012$ m, $r_{cc} = 0.25$ m, $R_{cc} = 0.35$ m, $L_{cc} = 0.3$ m. The red zone represents the cylindrical flame volume and blue circle denotes the position of the Dirac delta measurement function. The vertical dashed axis represents the longitudinal axis of the burner.

TABLE 2: FFD parameters of the control points for the annular combustor case

Volume	l	m	n
plenum	3	3	3
combustion chamber	3	3	6

ature in the plenum and premix ducts is constant at $\bar{T} = 1000$K. In the combustion chamber the temperature profile is parabolically decreasing between the values at the flame position and the chamber outlet, as shown in (20).

$$\bar{T}(z) = \begin{cases} 1000, & \text{if } z < z_f \\ (1000 - 2500)\left(\frac{z - z_f}{L_{cc}}\right)^2 + 2500, & \text{otherwise} \end{cases} \quad (20)$$

The speed of sound field is computed from the temperature distribution. We set a volumetric heat release rate within the red volume sketched in Fig. 6, in which each of the burners has an equal power ($q_0/20$). The heat release rate model is a $n - \tau$ model [23].

The inlet surface of the plenum and outlet surface of the combustion chamber are modelled as choked boundaries. The corresponding Mach numbers near the downstream and upstream ends of these boundaries are listed in Table 3. The reflection coefficients are calculated using Eq. (6) and Eq. (7).
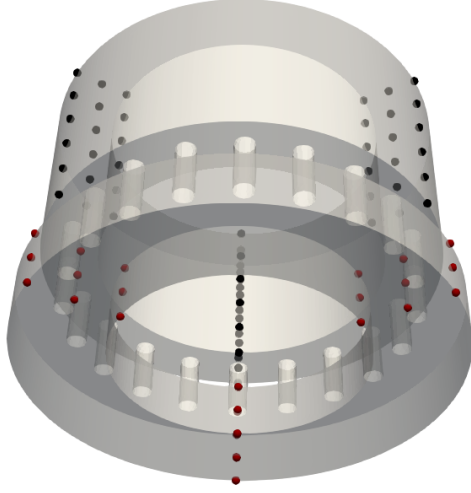
6

FIGURE 7: Free form deformation configuration for the LPP combustor. The red and black dots represent the control points for the plenum and combustion chamber.
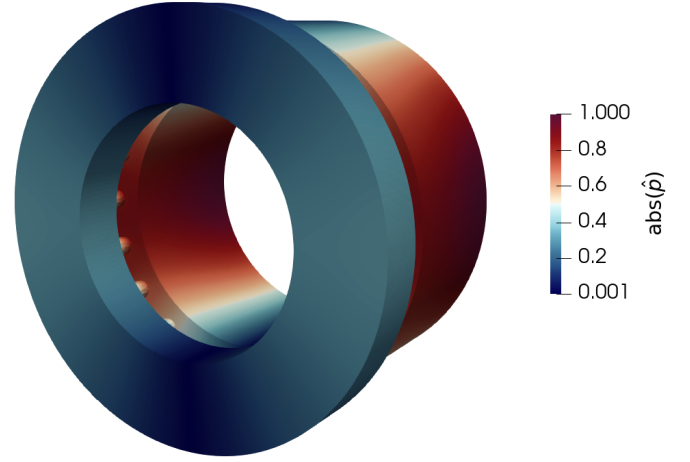

FIGURE 8: Normalized amplitude of the chamber-dominant azimuthal mode. The corresponding eigenfrequency is $\omega = 3296.713 + 533.272i$ rad s^{-1}

TABLE 3: Dimensional parameters of the annular combustor case

Parameter	value	unit
r_{gas}	287.1	Jkg^{-1}K^{-1}
$\bar{p}_{gas}$	50e5	Pa
$\bar{q}_0$	151.1	MW
$\bar{u}_b$	287.13	m s^{-1}
n	4.0	-
τ	0.0015	s
γ	1.4	-
$\bar{M}_{in}$	0.03	-
$\bar{M}_{out}$	0.07	-

4.2.3 Eigenmode. We are interested in the dominant azimuthal thermoacoustic mode of the LPP combustion chamber. The eigenfrequency of this configuration is found to be 524.688 Hz, which is close to that found with the low order network code in [25], at 520Hz. The calculated mode shape shown in Fig. 8 is also very similar to that in [25]. However, the growth rate found with our Helmholtz solver is different from than found in [8, 25] because the heat release rate is not pointwise, as it is in the low order network models.

4.2.4 Shape Modification. We obtain the direct and adjoint degenerate eigenmodes of the LPP combustor. For the FFD case of the LPP geometry, we consider radius changes for the lateral surfaces and axial changes for the inlet and outlet choked boundaries and symmetry-breaking changes are allowed. Our FFD framework does not take into account how geometry changes affect the flame behaviour. We therefore fix the premix duct geometry. We use Eq. (16) to compute the displacement field of the FFD control points. The example field representing the axial deformation of the FFD control point on the combustor outlet boundary is shown in Fig. 9.

These shape derivatives inform the changes made to the FFD points to reduce the growth rate. We deform the geometry it-
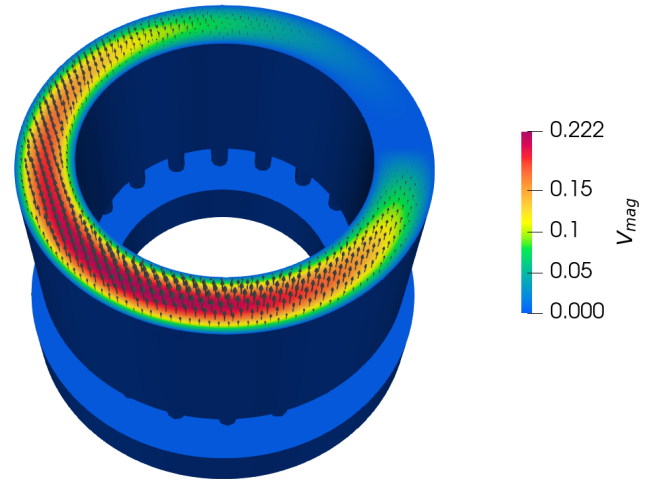

FIGURE 9: Deformation field of the LPP combustor for the control point P[i, j, k] where $i = 2, j = 2, k = 6$.

eratively following these shape derivatives. The resulting 3D geometry is shown in Fig. 10. Although the deformed geometry looks symmetrical, the rotational symmetry is slightly broken due to the differences between the shape derivatives along the circumferential direction. The eigenvalues of the deformed LPP geometry become $\omega_1 = 3251.7+405.2i$ and $\omega_2 = 3267.7+412.6i$ rad s^{-1}. The control points near the combustion chamber inlet are found to have more influence on the growth rate so the deformation magnitudes are large in that region. The smaller plenum together with bigger combustion chamber is more thermoacoustically stable than the original geometry.

The findings in this paper agree with [8] for the changes in the combustion chamber geometry but not the plenum geometry. This might be due to the inclusion of mean flow effects in [8], which are not included in this paper, or due to the compact flame assumption.

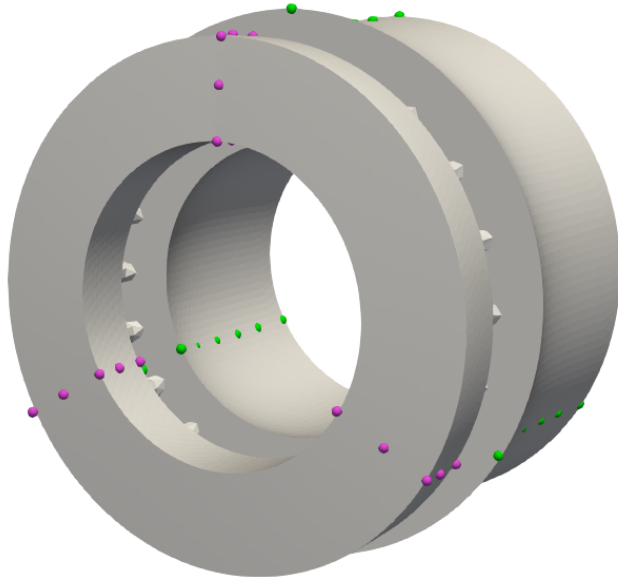The control points lying on the burner axis in Fig. 11 are

FIGURE 10: The 3D deformed geometry for the LPP combustor with its control points. The purple and green dots denote the positions of the FFD points after mesh deformation. The corresponding eigenvalues for deformed LPP geometry are $\omega_1 = 3251.7 + 405.2i$ and $\omega_2 = 3267.7 + 412.6i$ rad s^{-1}
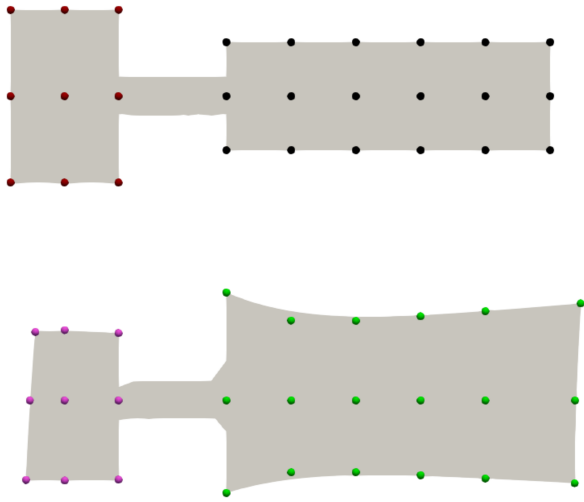

FIGURE 11: The sector slice of the initial (top) and deformed (bottom) geometry for the LPP combustor with its control points. The red and black dots denote the initial (top) positions of the FFD points while the purple and green dots denote the final (bottom) positions of the FFD points after mesh deformation. The positions of the control points on the burner axis kept unchanged, except the ones on the choked boundaries.

fixed, apart from the points on the choked boundaries. All the other control points are allowed to move. For the final geometry, the plenum volume became smaller while the combustion chamber volume is increased after FFD deformation. The thermoacoustic eigenvalues of the deformed LPP geometry have 24% lower growth rate than the initial case. This reduction could be increased by moving the points further.

5. CONCLUSION

In this study, we introduce free form deformation as a technique to reduce the instability of thermoacoustic systems. We find the shape derivatives of the eigenvalue with respect to the FFD control points using a 3D adjoint Helmholtz solver with only two calculations: the direct and adjoint eigenmodes. Then we impose mesh morphing with control point displacements by following the directions provided by the shape gradients at these points. We apply the FFD procedure to two different thermoacoustic systems: a Rijke tube and a model of a lean premixed prevaporized aeroengine combustor.

After moving the control points, we find that the deformed geometries have lower growth rates, as expected. This method is applicable to the plenum and combustion chamber for annular and can-annular geometries via local control lattices. Modification to the plenum may provide the most feasible option in practical cases because the plenum has a strong influence on the growth rate of thermoacoustic instabilities. We did not allow the burner geometries to change because the influence of the control points on the flame behaviour is not modelled.

The geometry parametrization shown in this paper will work straightforwardly on more complex gas turbine geometries. Together with damping models representing the acoustic damping caused by the dilution holes and liners, this framework could show how to reduce, or even eliminate, thermoacoustic instabilities in aircraft gas turbine engines.

REFERENCES

[1] Juniper, Matthew P. "Sensitivity analysis of thermoacoustic instability with adjoint Helmholtz solvers." *Physical Review Fluids* Vol. 3 No. 11 (2018): p. 110509.

[2] Zhao, Xinyu, Zhao, Dan, Cheng, Li, Shelton, Cody M and Majdalani, Joseph. "Predicting thermoacoustic stability characteristics of longitudinal combustors using different endpoint conditions with a low Mach number flow." *Physics of Fluids* Vol. 35 No. 9 (2023): pp. −.

[3] Bade, Stefanie, Wagner, Michael, Hirsch, Christoph, Sattelmayer, Thomas and Schuermans, Bruno. "Design for thermo-acoustic stability: modeling of burner and flame dynamics." *Journal of engineering for gas turbines and power* Vol. 135 No. 11 (2013): p. 111502.

[4] Bade, Stefanie, Wagner, Michael, Hirsch, Christoph, Sattelmayer, Thomas and Schuermans, Bruno. "Design for

thermo-acoustic stability: Procedure and database." *Journal of engineering for gas turbines and power* Vol. 135 No. 12 (2013): p. 121507.

[5] Magri, Luca. "Adjoint methods as design tools in thermoacoustics." *Applied Mechanics Reviews* Vol. 71 No. 2 (2019): p. 020801.

[6] Falco, Stefano and Juniper, Matthew P. "Shape optimization of thermoacoustic systems using a two-dimensional adjoint helmholtz solver." *Journal of Engineering for Gas Turbines and Power* Vol. 143 No. 7 (2021): p. 071025.

[7] Aguilar, José G and Juniper, Matthew P. "Thermoacoustic stabilization of a longitudinal combustor using adjoint methods." *Physical Review Fluids* Vol. 5 No. 8 (2020): p. 083902.

[8] Aguilar, José G and Juniper, Matthew P. "Adjoint methods for elimination of thermoacoustic oscillations in a model annular combustor via small geometry modifications." *Turbo Expo: Power for Land, Sea, and Air*, Vol. 51050: p. V04AT04A054. 2018. American Society of Mechanical Engineers.

[9] Ekici, Ekrem, Falco, Stefano and Juniper, Matthew P. "Shape sensitivity of thermoacoustic oscillations in an annular combustor with a 3D adjoint Helmholtz solver." *Computer Methods in Applied Mechanics and Engineering* Vol. 418 (2024): p. 116572.

[10] Sederberg, Thomas W and Parry, Scott R. "Free-form deformation of solid geometric models." *Proceedings of the 13th annual conference on Computer graphics and interactive techniques*: pp. 151–160. 1986.

[11] Samareh, Jamshid. "Aerodynamic shape optimization based on free-form deformation." *10th AIAA/ISSMO multidisciplinary analysis and optimization conference*: p. 4630. 2004.

[12] He, Xiaolong, Li, Jichao, Mader, Charles A, Yildirim, Anil and Martins, Joaquim RRA. "Robust aerodynamic shape optimization—from a circle to an airfoil." *Aerospace Science and Technology* Vol. 87 (2019): pp. 48–61.

[13] Giugno, Andrea, Shahpar, Shahrokh and Traverso, Alberto. "Adjoint-based optimization of a modern jet-engine fan blade." *Turbo Expo: Power for Land, Sea, and Air*, Vol. 84096: p. V02DT38A026. 2020. American Society of Mechanical Engineers.

[14] John, Alistair, Shahpar, Shahrokh and Qin, Ning. "Novel compressor blade shaping through a free-form method." *Journal of Turbomachinery* Vol. 139 No. 8 (2017): p. 081002.

[15] Li, Lei, Yuan, Tianyu, Li, Yuan, Yang, Weizhu and Kang, Jialei. "Multidisciplinary design optimization based on parameterized free-form deformation for single turbine." *AIAA Journal* Vol. 57 No. 5 (2019): pp. 2075–2087.

[16] Falco, Stefano. "Shape optimization for thermoacoustic instability with an adjoint Helmholtz solver." Ph.D. Thesis, University of Cambridge. 2022.

[17] Rienstra, Sjoerd W and Hirschberg, Avraham. "An introduction to acoustics." *Eindhoven University of Technology* Vol. 18 (2004): p. 19.

[18] Geuzaine, Christophe and Remacle, Jean-François. "Gmsh: A 3-D finite element mesh generator with built-in pre-and post-processing facilities." *International journal for numerical methods in engineering* Vol. 79 No. 11 (2009): pp. 1309–1331.

[19] Barrata, Igor A, Dean, Joseph P, Dokken, Jørgen S, HABERA, Michal, HALE, Jack, Richardson, Chris, Rognes, Marie E, Scroggs, Matthew W, Sime, Nathan and Wells, Garth N. "DOLFINx: The next generation FEniCS problem solving environment." - (2023): pp. –.

[20] Alnæs, Martin S, Logg, Anders, Ølgaard, Kristian B, Rognes, Marie E and Wells, Garth N. "Unified form language: A domain-specific language for weak formulations of partial differential equations." *ACM Transactions on Mathematical Software (TOMS)* Vol. 40 No. 2 (2014): pp. 1–37.

[21] Balay, Satish, Abhyankar, Shrirang, Adams, Mark, Brown, Jed, Brune, Peter, Buschelman, Kris, Dalcin, Lisandro, Dener, Alp, Eijkhout, Victor, Gropp, W et al. "PETSc users manual." - (2019): pp. –.

[22] Hernandez, Vicente, Roman, Jose E and Vidal, Vicente. "SLEPc: A scalable and flexible toolkit for the solution of eigenvalue problems." *ACM Transactions on Mathematical Software (TOMS)* Vol. 31 No. 3 (2005): pp. 351–362.

[23] Nicoud, Franck, Benoit, Laurent, Sensiau, Claude and Poinsot, Thierry. "Acoustic modes in combustors with complex impedances and multidimensional active flames." *AIAA journal* Vol. 45 No. 2 (2007): pp. 426–441.

[24] Gropp, William, Lusk, Ewing, Doss, Nathan and Skjellum, Anthony. "A high-performance, portable implementation of the MPI message passing interface standard." *Parallel computing* Vol. 22 No. 6 (1996): pp. 789–828.

[25] Morgans, Aimee S and Stow, Simon R. "Model-based control of combustion instabilities in annular combustors." *Combustion and flame* Vol. 150 No. 4 (2007): pp. 380–399.